The following supplement accompanies the article

Understanding differential patterns in coral reef recovery: chronic hydrodynamic disturbance as a limiting mechanism for coral colonization

T. Shay Viehman, James L. Hench, Sean P. Griffin, Amit Malhotra, Katharine Egan, Patrick N. Halpin

*Corresponding author: shay.viehman@noaa.gov

Marine Ecology Progress Series 605: 135–150

1. Benthic cover

Benthic cover was compared between the rubble, pavement, restoration and reference sites with planar photographs of permanent quadrats. Benthic cover was quantified using manual classification in CoralNet software (Beijbom et al. 2012). Classification categories included crustose coralline algae (CCA), coral, cyanobacteria, *Millepora* spp. hydrocoral, macroalgae, octocoral, other, bare substrate, sponges, and turf algae. Percentage values per quadrat were adjusted to exclude points landing on survey hardware. 105 photos were analyzed; however, photographs from 2009 and 2011 were not included due to lack of representation at all survey sites.

Throughout the study, rubble dominated the cover of substrate at the rubble site, and consolidated substrate dominated at all other sites (Fig. S1A). Turf algae dominated biological cover at all sites and years, although some annual variability was evident (reference site: 56.9 - 67.4%; restoration site: 57.4 - 81.6%; pavement site: 62.1% - 99%; 83.9 - 91.5%; Fig. S1B). The reference site had considerably higher macroalgal cover (0.5 - 26.9%; restoration site: 0.95 - 8.6%; pavement: 0.3 - 2.2%; rubble site: 0 - 1.65%; Fig. S1B). Cyanobacterial mats were present at the pavement and restoration sites in 2012 and 2013, and highest in 2012 at the pavement site (6.2%; Fig. S1B). Octocoral cover was highest 2.7 - 19.9% at the reference site, followed by the

restoration site (5.7 - 16.5%), pavement site (0.2 - 6.1%), and rubble site (0 - 2.9%), slightly higher than scleractinian coral cover in the reference (4.8 - 10.3%), restoration (3.3 - 4.3%), pavement (0 - 1.6%), and rubble sites (0 - 0.2%; Fig. S1B), although cover measurement of octocorals is imprecise with a planar approach using photographs.

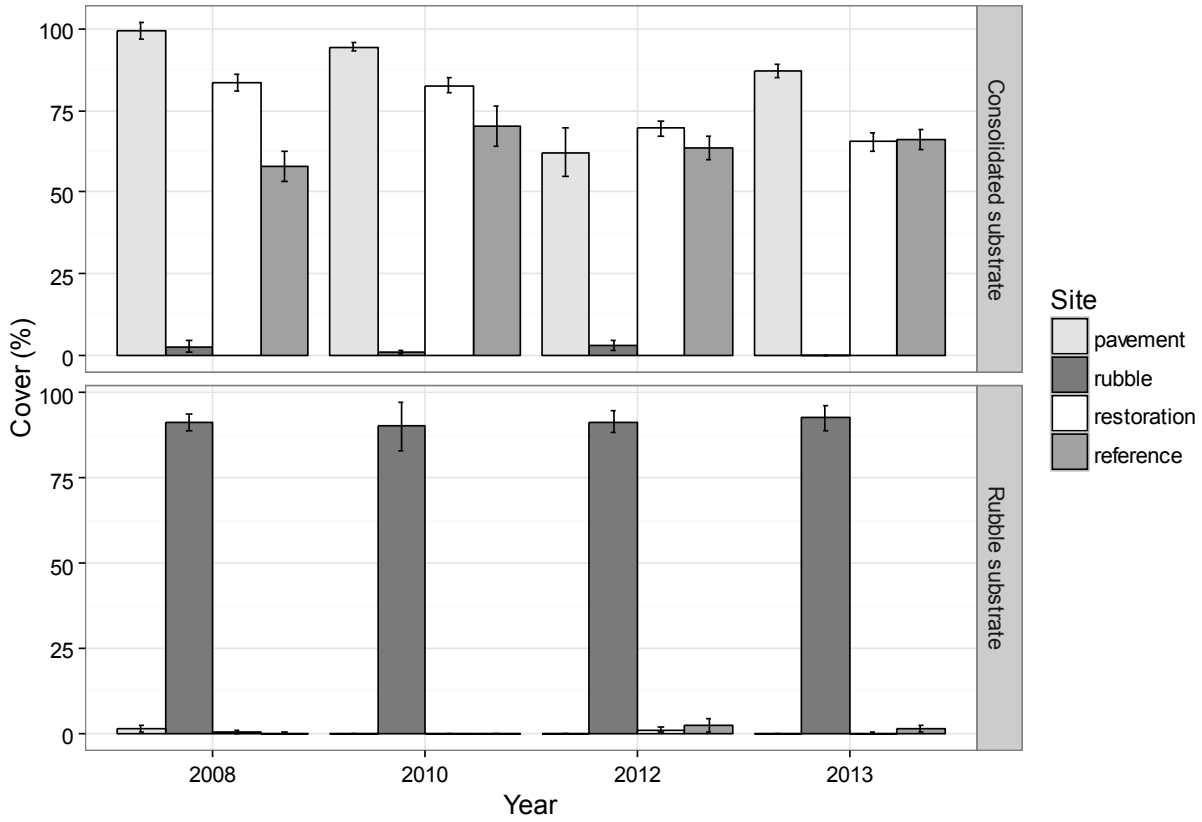

FIG. S1A. Mean cover (%) and standard error of substrate type for each sample level. No bar indicates zero cover. Years 2009 and 2011 are not included due to lack of field survey photographs at all levels.

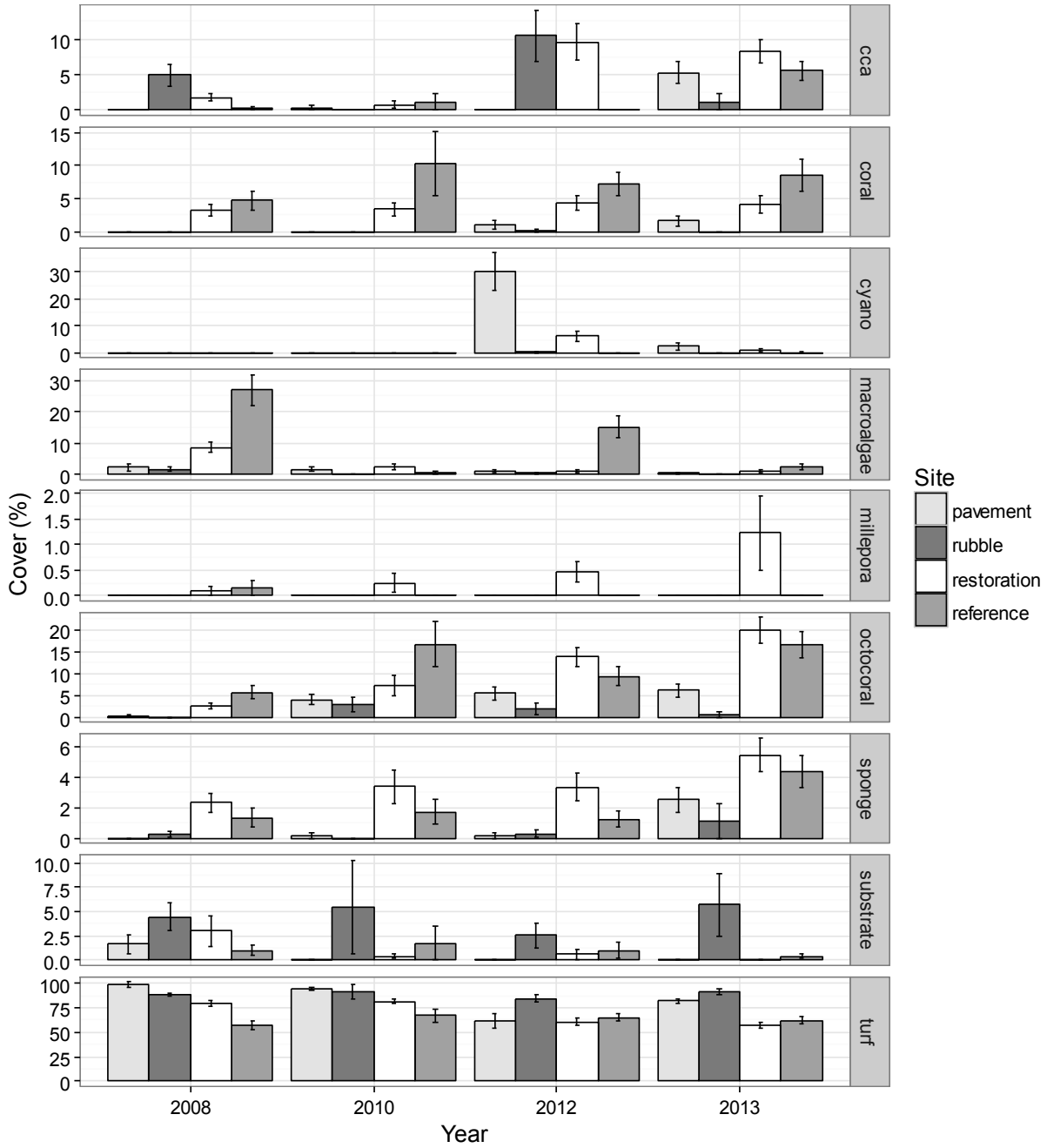

FIG. S1B. Mean cover (%) and standard error of benthic cover for each sample level. No bar indicates zero cover. Years 2009 and 2011 are not included due to lack of field survey photographs at all levels.

2. Temperature comparison

Near-bottom water temperatures (0.5 m above substrate) were measured at rubble and pavement sites during the intensive oceanographic measurement period (13 June – 17 July 2014) using high precision thermistors (Seabird SBE-56). Near bottom mean temperatures at the pavement site were 28.80 ± 0.22 °C and at the rubble site were 28.66 ± 0.22 °C, although the distribution of pavement site temperatures was skewed toward higher temperatures (Fig S2).

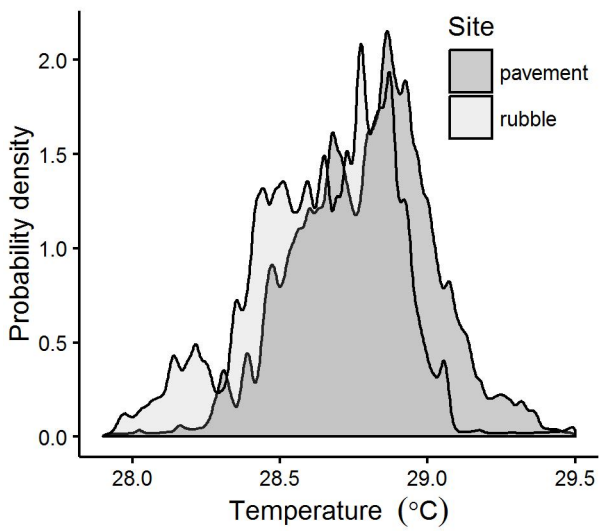

FIG. S2. Distribution of near-bottom water temperatures from thermistors (SBE56, Seabird Electronics) deployed at the rubble and pavement sites.

3. Wave model calibration and comparisons with field data

A systematic set of wave model simulations was conducted to test the sensitivity of model output to the model parameters for bottom roughness (k_w; value range tested: 0.01 - 1), as used in Madsen et al. (1988), and the wave breaking coefficient (γ_w; value range tested: 0.5 - 1) based on the bore model of Battjes and Janssen (1978). We also tested wave model sensitivity to inclusion of tidal forcing in the open boundary conditions, and inclusion of whitecapping effects based on Komen et al. (1984). Based on comparison with the field measurements, the optimal

wave model parameters were found to be k_w = 0.2 and γ_w = 0.6875. Model output at the three study sites was sensitive to the choice of bottom roughness, but was relatively insensitive to γ_w, not unsurprising given the relatively deep water depths at those sites, but also suggesting that breaking in other parts of model domain did not have a large effect on wave conditions at the three study sites. Application of time-varying water level increased overall model skill at each site by a negligible amount; however, tidal variation was not included in the final model hindcast runs because these forcing data were not available during the 4-year hindcast period.

4. Derivation of equations for rubble motion from external forces

We modeled the potential mobility of unconsolidated rubble within the disturbed areas using a mechanistic approach to estimate hydrodynamic forces required to initiate rubble motion. This approach has been well developed in the literature to hindcast hydrodynamic forcing required to mobilize boulders during large wave events (Nandasena et al. 2011). Here, a clast is approximated by an idealized cuboid (defined by *a*-, *b*-, *c*-axes) that is acted upon by gravity (F_g), normal (F_N), lift (F_L), friction (F_F), drag (F_D), and inertial (F_I) forces, where $F_F = \mu F_N$ and μ is the coefficient of static friction (Fig. 3). Hydrodynamic forcing exceeding a critical threshold can initiate rubble clast motion by sliding or over-turning. Sliding occurs when

$$F_D(t) + F_I(t) > \mu\left[F_g - F_L(t)\right] \tag{1}$$

At the initiation of sliding, the forces on the left and righthand side of Eq. (1) are equal. Forces that are functions of velocity (F_D, F_L, and F_I) vary with time (t) over a wave period. Grouping together terms that are quadratic in velocity gives

$$\left[F_D(t) + \mu F_L(t)\right] + F_I(t) - \mu F_g = 0 \tag{2}$$

The quadratic and lift forces due to waves are in phase with each other; however, they are both 90° out of phase with the inertial force. To estimate when rubble are mobilized, we are interested in when the total time-varying forces are maximum ($F_{T,m}$). Following the derivation of Dean and Dalrymple (1991), but extending it to include the lift force (2) can be represented as

$$F_{D,m} + \mu F_{L,m} + \frac{F_{I,m}^2}{4(F_{D,m} + \mu F_{L,m})} - \mu F_g = 0 \tag{3}$$

where the maximum drag force is,

$$F_{D,m} = \frac{1}{2}\rho_w C_D A_D U_m^2 \tag{4}$$

the maximum lift force is,

$$F_{L,m} = \frac{1}{2}\rho_w C_L A_L U_m^2 \tag{5}$$

the maximum inertial force is,

$$F_{I,m} = \rho_w C_M V (U_m \omega) \tag{6}$$

where $\omega = 2\pi / T$ is the wave frequency, T is the wave period, and V is the rubble volume. μ_s, C_D, C_L, and C_M are dimensionless coefficients of static friction, drag, lift, and mass respectively. A_D is the cross-sectional area of a rubble clast perpendicular to the flow and A_L is the area of a rubble clast parallel to the flow. The buoyant weight is,

$$F_g = \Delta\rho V g \tag{7}$$

where $\Delta\rho = \rho_r - \rho_w$, ρ_w is the density of seawater (1023 kg m^{-3}), ρ_r is rubble density, and g is acceleration due to gravity.

The water velocity can be decomposed intro contributions from current and waves (Grant & Madsen 1979)

$$U_m = U_c + U_w \tag{8}$$

Here we consider the case where currents are assumed to be constant (since current data are limited to the duration of the short-term field deployment), but waves vary with time (since wave hindcast data span 4-years),

$$U_m(t) = U_c + U_w(t) \tag{9}$$

Substituting the above expressions for the forces into (3), and noting that the currents do not contribute to the inertial force

$$\begin{aligned} &\tfrac{1}{2}\rho_w C_D A_D (U_c + U_w)^2 + \mu \tfrac{1}{2}\rho_w C_L A_L (U_c + U_w)^2 \\ &+ \frac{(\rho_w C_M V U_w \omega)^2}{4\left[\tfrac{1}{2}\rho_w C_D A_D (U_c + U_w)^2 + \mu \tfrac{1}{2}\rho_w C_L A_L (U_c + U_w)^2\right]} - \mu \Delta\rho V g = 0 \end{aligned} \tag{10}$$

We solve for U_w, the threshold wave orbital velocity for rubble sliding; all other variables have known values. To simplify notation, let

$$a = (\rho_w C_D A_D + \mu \rho_w C_L A_L) \tag{11}$$

$$b = \frac{(\rho_w C_M V \omega)^2}{\rho_w C_D A_D + \mu \rho_w C_L A_L} \tag{12}$$

$$c = -2\mu \Delta\rho V g \tag{13}$$

$$d = U_c \tag{14}$$

So that

$$a(d + U_w)^4 + b(U_w^2) + c(d + U_w)^2 = 0 \tag{15}$$

Expanding out polynomials and collecting like order terms yields a 4th order polynomial equation

$$(a)U_w^4 + (4ad)U_w^3 + (6ad^2 + b + c)U_w^2 + (4ad^3 + 2cd)U_w + (ad^4 + cd^2) = 0 \tag{16}$$

that we solved numerically and retained only physically realistic roots (*i.e.*, positive real numbers).

As an aside, note that for the case of no background mean current $(U_c = 0)$, equation (16) reduces to

$$U_m = \sqrt{\frac{\mu \frac{\Delta\rho}{\rho_w} Vg - \left[\frac{(C_M V \omega)}{2(C_D A_D + \mu C_L A_L)} \right] C_M V \omega}{\frac{1}{2}(C_D A_D + \mu C_L A_L)}} \tag{17}$$

Equation (17) is similar to Buckley et al. (2012)'s equation 6 for the threshold velocity of rubble motion, but with the addition of the term in grey, which represents a coefficient that accounts for the phasing required for the combined drag, lift, and inertial forces to be maximum. Simplifying (17) slightly gives an expression representing the threshold water velocity for rubble sliding,

$$u_{slide,m} = \sqrt{\frac{2\mu \frac{\Delta\rho}{\rho_w} Vg - \frac{(C_M V \omega)^2}{(C_D A_D + \mu C_L A_L)}}{(C_D A_D + \mu C_L A_L)}} \tag{18}$$

If $F_I > 2(F_D + F_L)$, then the total force is dominated by the inertial force, and (3) is replaced with the following equations (Dean and Dalrymple 1991)

$$F_{I,m} = \mu F_g \tag{19}$$

$$C_M V U_m \omega = \mu \Delta\rho V g \tag{20}$$

$$U_m = \frac{\mu \Delta\rho g}{C_M \omega} \tag{21}$$

And so for cases where $F_I > 2(F_D + F_L)$

$$u_{slide} = \frac{\mu \rho g}{C_M \omega} \tag{22}$$

Next we examine the case of rubble motion due to overturning. From the free-body diagram (Fig 3), rubble overturning occurs when the sum of the overturning moments exceed the restoring moment

$$F_D l_D + F_I l_I + F_L l_L > F_g l_g \tag{23}$$

where the moment arm for the drag and inertial forces are assumed to be the same (half the rubble height),

$$l_D = l_I = l_{rh} / 2 \equiv l_H \tag{24}$$

and the moment arm for the lift and gravitational forces are assumed to be the same (half the rubble width)

$$l_L = l_g = l_{rw} / 2 \equiv l_W \tag{25}$$

Substituting (24) and (25) into (23) and grouping terms

$$(F_D + F_I) l_H + (F_L - F_g) l_W = 0 \tag{26}$$

As in the derivation above for sliding, we are interested in time-varying overturning moments and so the internal force must be modified to account for relative phasing with drag and lift forces. Following Dean and Dalrymple (1991)

$$F_I = \frac{F_{I,m}^2}{4(F_{D,m} + F_{L,m})} \tag{27}$$

Substituting (27) and expressions for drag, lift, inertial and gravitational forces into (26) and simplifying gives

$$\begin{aligned} &\left(\rho_w^2 C_D^2 A_D^2 l_H + \rho_w^2 C_D C_L A_D A_L l_H + \rho_w^2 C_D C_L A_D A_L l_H + \rho_w^2 C_L^2 A_L^2 l_W\right) U_m^4 \\ &+\left(\rho_w^2 C_M^2 V^2 \omega^2 l_H - 2\rho_w C_D A_D \Delta\rho V g l_W - 2\rho_w C_L A_L \Delta\rho V g l_W\right) U_m^2 = 0 \end{aligned} \tag{28}$$

Then the overturning equation has the general quartic form where α and β are non-integers

$$\alpha U_m^4 + \beta U_m^2 = 0 \tag{29}$$

which was solved numerically for U_m, and only physically realistic roots retained.

5. Quantification of rubble morphology and sensitivity analyses

Rubble morphology was quantified to make force estimates in the rubble disturbance area by measuring surface area and buoyant weight from a random selection of rubble clasts collected from the rubble site in 2013 and 2014. Projected areas of individual clasts (n = 102) were measured along three dimensions: *a*-axis (top, length), *b*-axis (side, width) and *c*-axis (end, height) using orthogonal digital images and image analysis software (ImageJ; Rasband 1997; Fig S3). Area normal to flow (A_D) was considered to be along the *a*-axis; area perpendicular to flow (A_L) was considered to be along the plane of the *b*- and *c*-axes. Rubble volume (V) was calculated as the product of *a*-, *b*-, and *c*-axis lengths, where due to the irregular rubble shapes, each axis length was approximated as the square root of the corresponding area (*a*-*c*). Weights for dry and submerged rubble were measured using a digital force sensor (Vernier, Beaverton, OR), and buoyant weight was then calculated following Jokiel et al. (1978). In the general case, we use the median values of the range of measurements to determine effects of rubble properties on threshold bottom velocities for overturning (u_{over}) and sliding (u_{slide}) using (18) and (29). Sensitivity analyses were conducted with rubble property quantiles (5, 10, 25, 50, 75, 95%) from the distribution of each measurement (Fig S4). The smallest size class, at 5% rubble quartile, typically produced NA mobilization values.

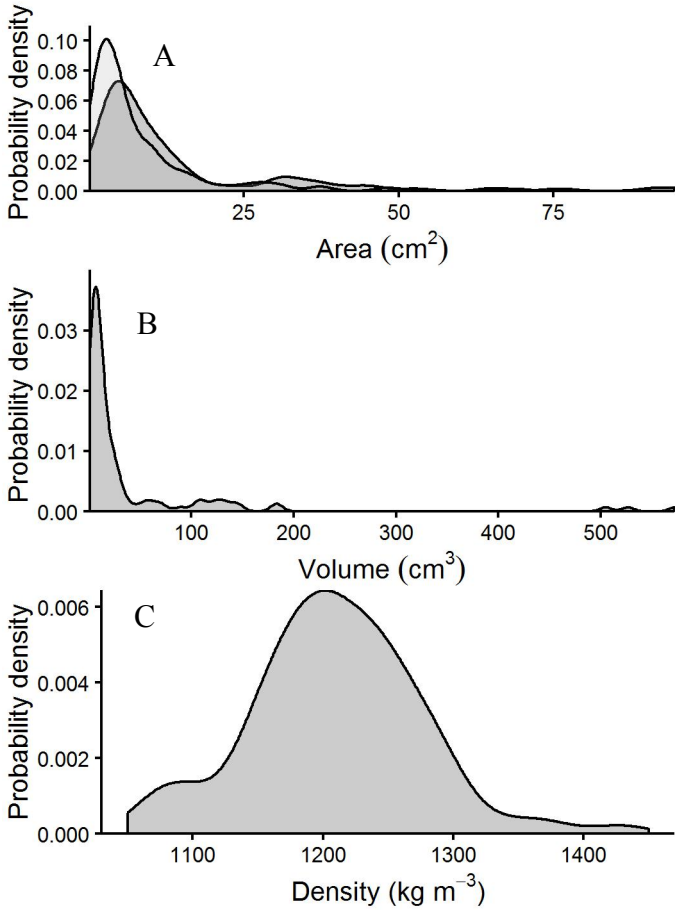

FIG. S3. Measured rubble A) area, B) volume, and C) density. In A) rubble area perpendicular to flow (A_D) is dark grey, and rubble area normal to the flow (A_L) is light grey.

In an expanse of reef rubble, proximity of multiple clasts likely impacts hydrodynamic forces affecting any given clast, due to enhanced friction from interlocking or by reduced area exposed to flow due to sheltering from adjacent objects. We addressed this by including a blocking term that accounts for reduction in A_D, following Storlazzi et al (2005). This term has a value from 0-1, corresponding to flow totally blocked to no blockage. We applied a value of 0.5 with recognition that a wide array of conditions is likely to exist in situ. Sensitivity analyses show little variability with a blockage value range from 0.1 to 0.9 (Fig. S4).

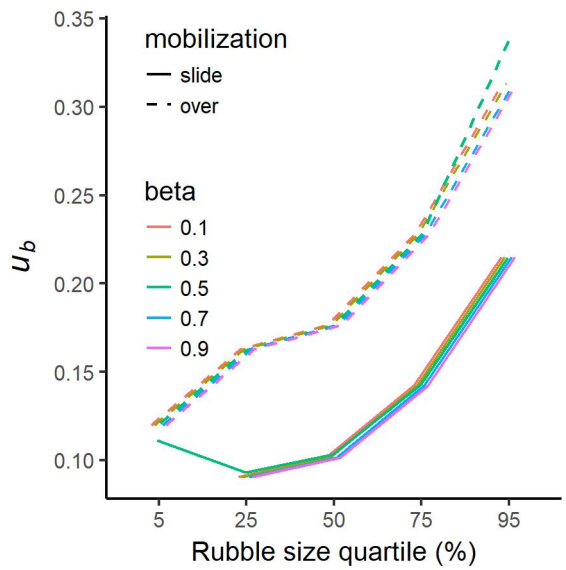

FIG. S4. Bottom orbital velocity (u_b) estimated to mobilize rubble through sliding or over turning, based on the distribution of rubble sizes (%) collected from within the rubble disturbance.

Summary statistics of rubble clast dimensions showed variability primarily in size and volume; sensitivity studies showed that the minimum bottom orbital velocity required to mobilize rubble was influenced by rubble size and exposure to flow (Fig. S5). Drag, lift, inertia and frictional forces estimated at each site were not significantly different between sites (Fig. S5), although the data suggest that the pavement sites had slightly higher forcing.

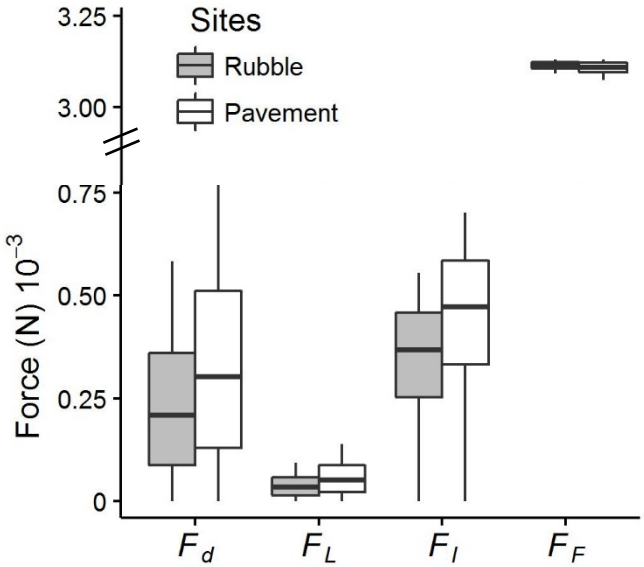

FIG. S5. Drag (F_d), lift (F_L), intertial (F_I) and frictional (F_F) forces estimated at the rubble and pavement sites, as calculated from mean rubble statistics and wave model output from 2010 - 2014. The box plot components are: solid line, median; box, interquartile range (IR); whiskers, most extreme point less than 1.5 times the IR from the median.

Literature cited

Battjes J, Janssen J (1978) Energy loss and set-up due to breaking of random waves. In: Proceedings 16th International Conference Coastal Engineering, ASCE.p 569–587

Beijbom O, Edmunds PJ, Kline DI, Mitchell BG, Kriegman D (2012) Automated annotation of coral reef survey images. In: 2012 IEEE Conference on Computer Vision and Pattern Recognition (CVPR).p 1170–1177

Buckley ML, Wei Y, Jaffe BE, Watt SG (2012) Inverse modeling of velocities and inferred cause of overwash that emplaced inland fields of boulders at Anegada, British Virgin Islands. Nat Hazards 63:133–149 https://doi.org/10.1007/s11069-011-9725-8

Cheng N, Chiew Y (1998) Pick-up probability for sediment entrainment. J Hydraul Eng ASCE 124:232–235 https://doi.org/10.1061/(ASCE)0733-9429(1998)124:2(232)

Dean RG, Dalrymple RA (1991) Water Wave Mechanics for Engineers and Scientists. World Scientific, Singapore

Goto K, Chavanich SA, Imamura F, Kunthasap P, Matsui T, Minoura K, Sugawara D, Yanagisawa H (2007) Distribution, origin and transport process of boulders deposited by the 2004 Indian Ocean tsunami at Pakarang Cape, Thailand. Sediment Geol 202:821–837 https://doi.org/10.1016/j.sedgeo.2007.09.004

Grant W, Madsen O (1979) Combined wave and current interaction with a rough bottom. J Geophys Res Oceans 84:1797–1808 https://doi.org/10.1029/JC084iC04p01797

Imamura F, Goto K, Ohkubo S (2008) A numerical model for the transport of a boulder by tsunami. J Geophys Res Oceans 113:C01008 https://doi.org/10.1029/2007JC004170

Jokiel PL, Maragos J, Franzisket L (1978) Coral Reefs: Research Methods. In: Stoddart DR, Johannes RE (eds) Coral growth: buoyant weight technique. UNESCO, Paris, p 529–541

Komen G, Hasselmann S, Hasselmann K (1984) On the existence of a fully developed wind-sea spectrum. J Phys Oceanogr 14:1271–1285 https://doi.org/10.1175/1520-0485(1984)014<1271:OTEOAF>2.0.CO;2

Madsen O, Poon Y-K, Graber H (1988) Spectral wave attenuation by bottom friction: theory. In: Proceedings 21th International Conference Coastal Engineering, ASCE.p 492–504

Noormets R, Crook KAW, Felton EA (2004) Sedimentology of rocky shorelines: 3.: Hydrodynamics of megaclast emplacement and transport on a shore platform, Oahu, Hawaii. Sediment Geol 172:41–65

Nott J (2003) Waves, coastal boulder deposits and the importance of the pre-transport setting. Earth Planet Sci Lett 210:269–276 https://doi.org/10.1016/S0012-821X(03)00104-3

Paris R, Wassmer P, Sartohadi J, Lavigne F, Barthomeuf B, Desgages E, Grancher D, Baumert P, Vautier F, Brunstein D, Gomez C (2009) Tsunamis as geomorphic crises: Lessons from the December 26, 2004 tsunami in Lhok Nga, West Banda Aceh (Sumatra, Indonesia). Geomorphology 104:59–72 https://doi.org/10.1016/j.geomorph.2008.05.040

Rasband WS (1997) ImageJ: Image Processing and Analysis in Java. U.S. National Institutes of Health, Bethesda, Maryland, USA

Storlazzi CD, Brown EK, Field ME, Rodgers K, Jokiel PL (2005) A model for wave control on coral breakage and species distribution in the Hawaiian Islands. Coral Reefs 24:43–55 https://doi.org/10.1007/s00338-004-0430-x

Voropayev SI, Cense AW, McEachern GB, Boyer DL, Fernando HJS (2001) Dynamics of cobbles in the shoaling region of a surf zone. Ocean Eng 28:763–788 https://doi.org/10.1016/S0029-8018(00)00032-9